Optics Letters

Influence of the sampling clock pulse shape mismatch on channel-interleaved photonic analog-to-digital conversion

GUANG YANG, WEIWEN ZOU,* LEI YU, AND JIANPING CHEN

State Key Laboratory of Advanced Optical Communication Systems and Networks, Shanghai Institute for Advanced Communication and Data Science, Department of Electronic Engineering, Shanghai Jiao Tong University, Shanghai 200240, China
**Corresponding author: wzou@sjtu.edu.cn*

Received 21 May 2018; revised 19 June 2018; accepted 20 June 2018; posted 21 June 2018 (Doc. ID 332182); published 19 July 2018

We investigate the pulse shape mismatch of the sampling clock in channel-interleaved photonic analog-to-digital converters (PADCs) and its influence on the frequency response of the PADC system. Two schemes to generate sampling clock pulses are experimentally implemented to study the influence of the pulse shape mismatch. The scheme with the well-managed pulse shape in all channels is successful in eliminating the influence. Subsequently, a flat 35 GHz frequency response of a four-channel 40 GSa/s PADC is demonstrated, and the effective number of bits reaches 7.7 bits at 11 GHz and 7 bits at 31 GHz.

OCIS codes: (060.5625) Radio frequency photonics; (230.0250) Optoelectronics; (250.4745) Optical processing devices; (000.4430) Numerical approximation and analysis.

https://doi.org/10.1364/OL.43.003530

Next-generation radar systems are demanding for the reception and processing of ultra-wideband signals at high frequency bands [1,2]. With ultra-wideband analog input and a high sampling rate, photonic analog-to-digital conversion (PADC) technology provides a feasible solution [3,4]. One typical PADC with a high sampling rate and high resolution is called the photonic sampled and electronic digitized PADC [5–12]. The analog input is first received by a photonic front end and converted and digitized by an electronic back end. Recently, this kind of PADC has been adopted and verified in demonstration of the photonics-based radar system [1], which brings new opportunity for microwave photonics to serve next-generation radar systems [13,14].

A next-generation radar system will work at different frequency bands with various bandwidths. Hence, the flat frequency response is necessary for the radar receiver, and the sampling rate should satisfy the requirement of the input bandwidth. Thus, the PADC originating from a sampling clock with the low timing jitter always needs to be channel-interleaved to multiply the sampling rate. In other words, the optical pulse train of a PADC needs to be demultiplexed into multiple parallel channels to reduce the demand of the bandwidth and sampling rate of the electronic back end in each channel. To date, several channel-interleaved methods have been proposed based on different schemes of sampling clock generation [6–12]. Recently, the influence of the sampling clock on the frequency response in a single-channel PADC system (i.e., a standard microwave photonic link) has been studied in [15,16]. However, in the channel-interleaved architecture, the pulse shape of the sampling clock would be distorted [8] and result in the channel mismatches to the PADC system.

In this Letter, we investigate the essential influence of the pulse shape mismatch of the sampling clock on the frequency response in the channel-interleaved PADC system. When the pulse shapes of all channels are well managed, the influence of the pulse shape mismatch is effectively eliminated. A flat response within the frequency range of 35 GHz is experimentally achieved in a 40 GSa/s PADC system.

The schematic of the channel-interleaved PADC systems is shown in Fig. 1, including a photonic front end and an electronic back end. In the photonic front end, the analog input signal is sampled at the sampling rate of f_s by electronic-optical (E/O) modulation (i.e., electro-optic modulator). Later, the pulse train is demultiplexed into N parallel channels via a demultiplexer (DEMUX). Note that the DEMUX can be a time-domain or wavelength-domain demultiplexer, according to the sampling clock generation method, which will be explained below. In the electronic back end, the demultiplexed pulse trains

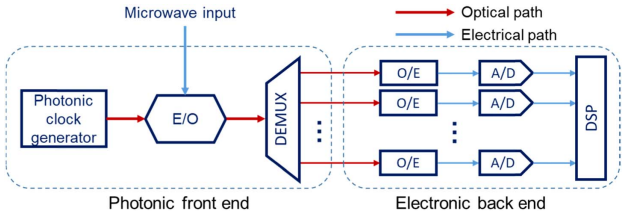

Fig. 1. Schematic of channel-interleaved PADC. E/O, electro-optical modulation; DEMUX, demultiplexer; O/E, optical-electronic conversion; A/D, analog-to-digital conversion; DSP, digital signal processor.

Table 1. Denotations of Parameters in Eq. (1)

Temporal Response	Spectral Response	Denotation
$v_{\text{in}}(t)$	$V_{\text{in}}(f)$	Analog input
$h_{\text{EO}}(t)$	$H_{\text{EO}}(f)$	Frequency response of electro-optical modulation
$s_n(t)$	$S_n(f)$	Sampling clock in the nth channel
$h_{\text{OE}}(t)$	$H_{\text{OE}}(f)$	Frequency response of electronic back end
$v_{\text{out}}(t)$	$V_{\text{out}}(f)$	Digitized output

are first converted into electronic signals by an array of photodetectors (PDs), which is also nominated as optical-electronic (O/E) conversion. The converted electronic signal is digitized by an array of electronic ADCs. Finally, the digitized data are reconstructed via a channel-mapping algorithm, which has been introduced in [9] by a digital signal processor (DSP) or personal computer to achieve the sampling rate of f_s.

In mathematics, the temporal and spectral responses of the channel-interleaved PADC can be expressed as follows:

$$\begin{cases} v_{\text{out}}(t) = \sum_{n=1}^{N} h_{\text{OE}}(t) * \{[h_{\text{EO}}(t) * v_{\text{in}}(t)] \times s_n(t)\} \\ V_{\text{out}}(f) = \sum_{n=1}^{N} H_{\text{OE}}(f) \times \{[H_{\text{EO}}(f) \times V_{\text{in}}(f)] * S_n(f)\} \end{cases}, \tag{1}$$

where N is the number of interleaved channels, * denotes the convolution, and the denotations of the other parameters are expanded in Table 1.

The photonic sampling clock in the nth channel can be further written by

$$\begin{cases} s_n(t) = p_n(t) * \sum_{m=-\infty}^{\infty} \delta[t - mNT_s - (n-1)T_s] \\ p_n(t) = p(t) + e_n(t) \end{cases}, \tag{2}$$

where $T_s = 1/f_s$, $p_n(t)$ is the pulse shape in the nth channel after demultiplexing, m is the index of the pulses in the pulse train, $p(t)$ is the average of $p_n(t)$, and $e_n(t) = p_n(t) - p(t)$ represents the pulse shape mismatch of the nth channel from the averaged pulse shape.

In the theoretical analysis, we assume that the bandwidth of the electronic back end is within the single-channel Nyquist bandwidth (i.e., $f_s/2N$). For a single tone input of $v_{\text{in}}(t) = v_0 \exp(j2\pi f_0 t)$ at the frequency of f_0, the spectrum of the digitized data in a single channel can be derived from Eqs. (1) and (2), which is described by

$$V_{out}(f) = A_S \delta(f_0 - k' f_s) + \sum_{m=1}^{N-1} A_{D,m} \delta(f_0 - k' f_s - m f_s/N), \quad \text{where} \begin{cases} A_{D,m} = (V_0/N) \sum_{n=1}^{N} E_n(k f_s/N) e^{-j2\pi m(n-1)/N} \\ A_S = V_0 P(k f_s/N) \\ V_0 = v_0 H_{\text{EO}}(f_0) H_{\text{OE}}(f_0 - k f_s/N) \end{cases}, \tag{3}$$

where $P_n(f)$, $P(f)$, and $E_n(f)$ are the spectra of $p_n(t)$, $p(t)$, and $e_n(t)$, respectively; and k and k' are integers satisfying $-f_s/2N < f_0 - k f_s < f_s/2N$, and $-f_s/2 < f_0 - k' f_s < f_s/2$, respectively. It can be found that the pulse shape mismatch induces the distortion spurs in the spectrum. Consequently, the normalized power of the distortions induced by pulse shape mismatch (Δ_P) can be calculated by

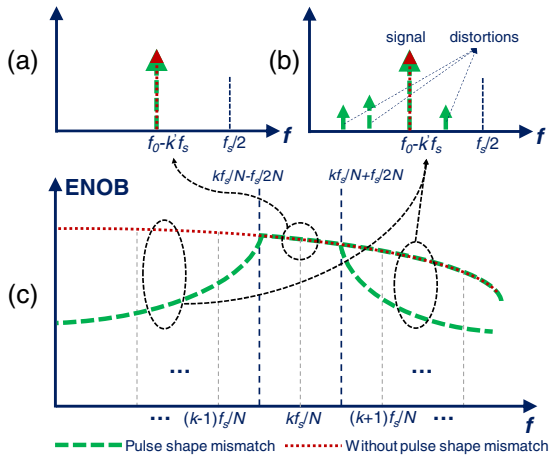

Fig. 2. Pulse shape influence on channel-interleaved PADC. The spectra (a) within or (b) out of the frequency range of the effective channel compensation. (c) Frequency response of the ENOB with/without the pulse shape mismatch.

$$\Delta_P = \sum_{m=1}^{N-1} A_{D,m}^2 / A_S^2. \tag{4}$$

Combining Eq. (4) with the theoretical analysis in [9], the signal-to-noise-and distortion ratio (SINAD) can be revised as

$$\text{SINAD} = -10 \log[\sigma_a^2 + \sigma_N^2 + 4\pi^2 f_0^2 (\sigma_t^2 + \sigma_J^2) + \Delta_P], \tag{5}$$

where σ_a is the normalized root-mean-square (RMS) amplitude mismatch, σ_t is the RMS clock timing mismatch, σ_J is the RMS clock timing jitter, and σ_N represents the normalized amplitude noise power. The effective number of bits (ENOB) can be derived as ENOB = (SINAD − 1.76)/6.02.

From Eq. (3), it can be found that the spectral distortions induced by the pulse shape mismatch depend on the integer k, which makes Δ_P in Eq. (4) vary with the input frequency f_0. Hence, the SINAD and ENOB changes with f_0, deteriorating the flatness of the frequency response. For a specific integer k in Eq. (3), the pulse shape mismatch can be possibly compensated for by [8]

$$\begin{cases} P_n^*(f) = a_n P_n(f), n = 1, 2, \ldots, N \\ P_1^*(k f_s/N) = P_2^*(k f_s/N) = \ldots = P_N^*(k f_s/N) \end{cases}, \tag{6}$$

where a_n represents the amplitude tuning coefficient in the nth channel. If $P_n(f)$ in Eq. (3) is substituted by $P_n^*(f)$, it could be found that the amplitude mismatch is effectively compensated for the input frequencies in the frequency range of $-f_s/2N < f_0 - k f_s/N < f_s/2N$, as illustrated in Fig. 2(a). However, due to the pulse shape mismatch, the fixed set of coefficients a_n cannot enable the compensation for f_0 lying

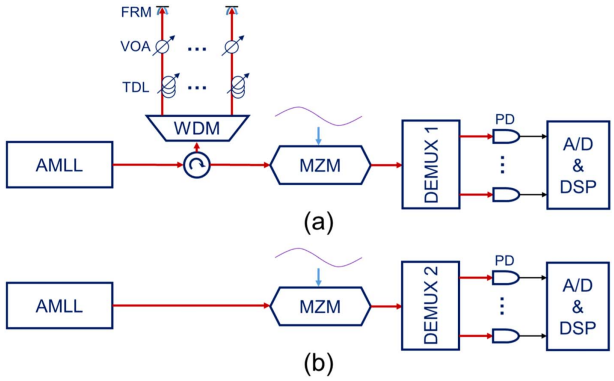

Fig. 3. Experimental setup of channel-interleaved PADC with two methods of sampling clock generation. (a) Time-wavelength interleaving method, (b) direct generation. FRM, Faraday rotating mirror; VOA, variable optical attenuator; TDL, tunable delay line; PD, photodetector; DEMUX, demultiplexer.

out of the above frequency range. The spectrum in this case is schematically depicted in Fig. 2(b). Furthermore, a schematic of PADC frequency response in terms of ENOB calculated from Eq. (5) is shown in Fig. 2(c). Subsequently, the flatness of the frequency response are degenerated by the uneven effectiveness of compensation.

Two experimental setups with different schemes of sampling clock generation are illustrated in Fig. 3. In scheme 1, shown in Fig. 3(a), the clock is seeded by an actively mode-locked laser (AMLL, Calmar PSL-10-TT) and then sliced into multiple channels by a wavelength division multiplexer (WDM). These channels are mapped in the time domain to generate the sampling clock [8], and the pulse train of samples is demultiplexed via another WDM. Scheme 2 is depicted in Fig. 3(b). The sampling clock is directly generated from the AMLL (Calmar PSL-40-TT). The pulse train of samples is parallelized via a network of photonic switches which are driven by microwave signals divided from the sampling clock [11]. Meanwhile, the inherent symmetry of these switches produces well-managed pulse shapes in all demultiplexed channels. It is worth noting that the on-off ratio of these switches is >30 dB in optical power, which could support a high resolution in digitization [12].

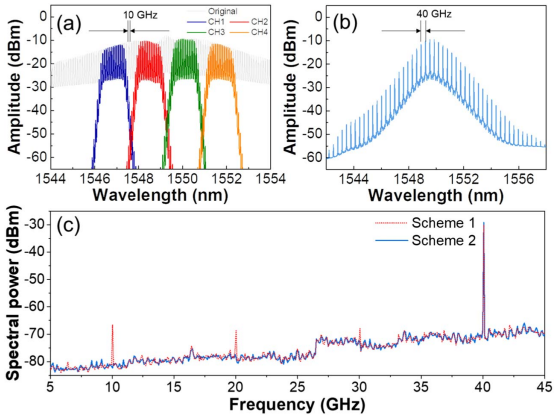

Fig. 4. Optical spectra of 40 GSa/s sampling clock from (a) time-wavelength interleaving (scheme 1) and (b) direct generation (scheme 2). (c) Microwave spectra of the sampling clock in (a) and (b).

Both schemes are set at the sampling rate of 40 GSa/s. In scheme 1, the spectrum of 10 GHz AMLL is first broadened by a pulse compressor (Calmar PCS-2) and then sliced into four channels, as shown in Fig. 4(a). The sampling rate is time-mapped to 40 GSa/s. The repetition rate of the AMLL in scheme 2 is 40 GHz, directly providing the 40 GSa/s sampling clock. Its optical spectrum is depicted in Fig. 4(b). The microwave spectra of the sampling clock in both schemes are depicted in Fig. 4(c), which are measured by an RF spectral analyzer (R&S FSUP 50) via a PD with a 50 GHz bandwidth (Finisar XPDV2150R). It can be found that there are three obvious spurs (10, 20, and 30 GHz) in scheme 1, whereas there is no spur in scheme 2. Note that the amplitude and time delay among four channels in scheme 1 have been tuned optimally [8]. However, due to the limited precision of the tuning hardware and spectral mismatch of the WDM channels, the pulse shape mismatch always appears.

The analog input is sampled by the photonic clock via a MZM with a 40 GHz input bandwidth (Photoline MXIQ-LN-40). The O/E conversion of the demultiplexed pulse trains of samples is performed by an array of PDs (Beijing Conquer, KG-PT-3G) with 3 GHz bandwidths and digitized by a 10 GSa/s four-channel oscilloscope (Keysight MSO804A) that is synchronized to the AMLL. The EADCs of the oscilloscope have 12 digitization bits, and their ENOB can be up to 8.7 [17]. The AMLLs in both schemes are seeded by the same microwave synthesizer to achieve a comparable timing jitter, and the optical power in both schemes is managed to get similar amplitude noise level in the electronic back end. To analyze the mismatch distortions, the digitized data are transformed to the spectra, which are illustrated in Fig. 5. The original spectra are depicted in Figs. 5(a) and 5(b) and compared with the spectra after compensation in Figs. 5(c)–5(h). Since the timing jitter and amplitude noise in both schemes are comparable, the original spectra from scheme 1 are illustrated, which are almost

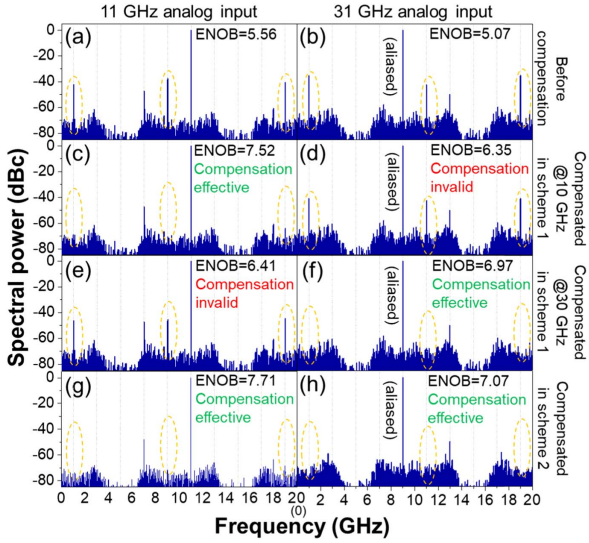

Fig. 5. Spectra of the digitized data of 11 and 31 GHz analog input. (a) and (b) Before compensation. (c) and (d) Effective compensation by the coefficients valid around 10 GHz in scheme 1. (e) and (f) Effective compensation by the coefficients valid around 30 GHz in scheme 1. (g) and (h) Compensation in scheme 2. Note that 31 GHz is aliased to 9 GHz.

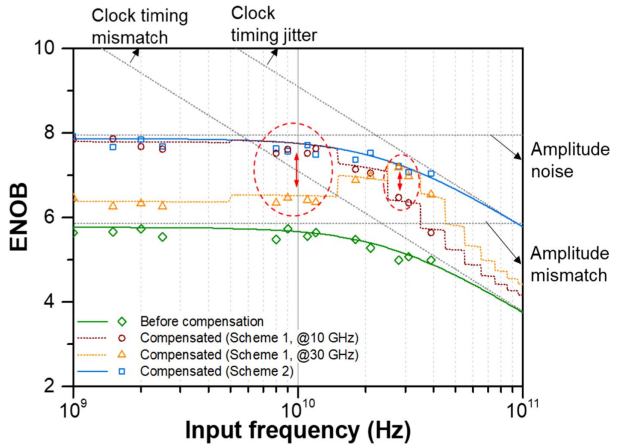

Fig. 6. ENOB versus the input frequency in both schemes. The curves are the theoretical estimations, and the symbols are the experimental results. The values around 10 and 30 GHz are circled out for clear comparison.

identical to that of scheme 2. It should be noted that the compensation is based on the channel-mapping algorithm [9]. It can be found that the 31 GHz input is aliased to 9 GHz in the sub-sampling performed by the 40 GSa/s PADC. In a single channel, the 31 GHz input is folded to 1 GHz, which can be detected via the 3 GHz PD. Figures 5(c)–5(f) illustrate the compensated spectra of 11 and 31 GHz analog input in scheme 1. The results of scheme 2 are shown in Figs. 5(g) and 5(h), respectively. Note that the locations of the distortion spurs are circled out. It can be found that in scheme 2, one set of compensation coefficients is effective for both analog inputs at 11 and 31 GHz to eliminate the distortion spurs. However, for scheme 1, the compensation with the coefficients valid for 11 GHz becomes invalid for the 31 GHz input and vice versa. Besides, it is worth noting that in the cases where the compensation is degenerated, the distortion spurs are still slightly reduced, since the mismatches in amplitude and time delay are optimally compensated for, and there remains only the influence of pulse shape mismatch of the sampling clock.

The ENOB can be derived from the spectra of the digitized data. The experimental results of the ENOB are illustrated in Fig. 6 and compared with the theoretical estimations which can be derived based on Eq. (5). Note that the parameters for the theoretical estimations are properly set according to the experimental conditions: $\sigma_a = 1 \times 10^{-4}$, $\sigma_t = 95$ fs, $\sigma_N = 1.4 \times 10^{-4}$, and $\sigma_J = 36$ fs; and Δ_P is derived via Eq. (4) with the transform-limit pulse shapes of the spectra in Fig. 4. The ENOB is essentially limited by the channel mismatch and can be enhanced to the limitation of noise and timing jitter after compensation [9]. The enhancement of ENOB can be used to indicate the effectiveness of the channel compensation. It can be found that the compensation in scheme 2 remains effective in the whole frequency range of 35 GHz. However, for scheme 1, the compensation with coefficients valid for 10 or 30 GHz is only valid in the range of $5 \sim 15$ or $25 \sim 35$ GHz, respectively. This indicates that the compensation in scheme 1 with coefficients derived around kf_s/N can be only feasible in the range of $-f_s/2N < f_0 - kf_s/N < f_s/2N$ ($f_s = 40$ GHz, $N = 4$, $k = 1$ or 3 in the experiment), matching well with the theoretical analysis in Eq. (6). Therefore, the flatness of the frequency response represented by the ENOB is degenerated by the pulse shape mismatch in scheme 1. In comparison, the ENOB in scheme 2 addicts to the theoretical limitation and guarantees the flatness of the frequency response owing to the well-managed pulse shape of the sampling clock.

In conclusion, we have investigated the influence of the pulse shape mismatch of photonic sampling clock in the channel-interleaved PADC system. The pulse shape mismatch is theoretically and experimentally analyzed in two schemes with different methods of sampling clock generation. The influence of pulse shape mismatch is clarified by the degenerated flatness of the frequency response of the PADC system. In a four-channel 40 GSa/s scheme with well-managed pulse shapes, a flat frequency response within 35 GHz is experimentally demonstrated, and the ENOB reaches 7.7 bits at 11 GHz and 7.0 bits at 31 GHz. Since the detection of a broadband signal is different from that of single-frequency input [10], we will investigate the effectiveness of the PADC with well-managed pulse shapes to the ultra-broad instantaneous bandwidth for the practical application of next-generation broadband radar.

Funding. National Natural Science Foundation of China (NSFC) (61535006, 61571292); Science and Technology Commission of Shanghai Municipality (STCSM).

REFERENCES

1. P. Ghelfi, F. Laghezza, F. Scotti, and G. Serafino, A. Capria, S. Pinna, D. Onori, C. Porzi, M. Scaffardi, A. Malacarne, V. Vercesi, E. Lazzeri, and A. Bogoni, Nature **507**, 341 (2014).
2. W. Zou, H. Zhang, X. Long, S. Zhang, Y. Cui, and J. Chen, Sci. Rep. **6**, 19786 (2016).
3. G. C. Valley, Opt. Express **15**, 1995 (2007).
4. A. Khilo, S. J. Spector, M. E. Grein, A. H. Nejadmalayeri, C. W. Holzwarth, M. Y. Sander, M. S. Dahlem, M. Y. Peng, M. W. Geis, N. A. DiLello, J. U. Yoon, A. Motamedi, J. S. Orcutt, J. P. Wang, C. M. Sorace-Agaskar, M. A. Popović, J. Sun, G. Zhou, H. Byun, J. Chen, J. L. Hoyt, H. I. Smith, R. J. Ram, M. Perrott, T. M. Lyszczarz, E. P. Ippen, and F. X. Kärtner, Opt. Express **20**, 4454 (2012).
5. J. Kim, M. J. Park, M. H. Perrott, and F. X. Kärtner, Opt. Express **16**, 16509 (2008).
6. A. Yariv and R. G. M. P. Koumans, Electron. Lett. **34**, 2012 (1998).
7. T. R. Clark, J. U. Kang, and R. D. Esman, IEEE Photonics Technol. Lett. **11**, 1168 (1999).
8. G. Yang, W. Zou, X. Li, and J. Chen, Opt. Express **23**, 2174 (2015).
9. G. Yang, W. Zou, L. Yu, K. Wu, and J. Chen, Opt. Express **24**, 24061 (2016).
10. G. Yang, W. Zou, Y. Yuan, and J. Chen, Chin. Opt. Lett. **16**, 030601 (2018).
11. F. Scotti, F. Laghezza, S. Pinna, P. Ghelfi, and A. Bogoni, *OptoElectronics and Communications Conference and Photonics in Switching* (Optical Society of America, 2013), paper TuO1_3.
12. L. Yu, W. Zou, G. Yang, X. Li, and J. Chen, *International Topical Meeting on Microwave Photonics* (2017), paper THP.29.
13. J. Capmany and D. Novak, Nat. Photonics **1**, 319 (2007).
14. J. Yao, J. Lightwave Technol. **27**, 314 (2009).
15. F. Su, G. Wu, W. Zou, and J. Chen, arXiv:1604.01427 (2016).
16. F. Su, G. Wu, and J. Chen, Opt. Lett. **41**, 2779 (2016).
17. Keysight Technologies, "Infiniium S-series high-definition oscilloscopes—data sheet," 2018, http://literature.cdn.keysight.com/litweb/pdf/5991-3904EN.pdf.